Modal Analysis of Photonic Crystal Double-Heterostructure Laser Cavities

Adam Mock, *Student Member, IEEE*, Ling Lu, *Student Member, IEEE*, Eui Hyun Hwang,
John O'Brien, *Senior Member, IEEE*, and P. Daniel Dapkus, *Fellow, IEEE*

Abstract—A detailed 3-D finite-difference time-domain analysis of photonic crystal double-heterostructure bound state resonances is presented along with supporting experimental results. The connection between different photonic crystal waveguide bands and the associated photonic crystal double-heterostructure bound states is made, and mode profiles are presented. We analyze the quality factors using the Padé interpolation method and directional radiation properties by calculating the time-averaged Poynting vector. We also present field profiles of higher order bound states and discuss cavity geometries to enhance a given bound state mode relative to neighboring modes. Experimental lasing results are presented demonstrating the utility of our approach.

Index Terms—Finite-difference time-domain (FDTD) methods, integrated optics, photonic bandgap materials, quality factor, resonators, semiconductor laser.

I. INTRODUCTION

SINCE the first theoretical investigations of devices employing photonic crystal patterns with spatially varying attributes [1]–[3], such photonic crystal heterostructures have shown promise for chip-scale optical information processing applications [4]–[6]. Photonic crystal double-heterostructure devices in which a photonic "well" is introduced into an otherwise uniform lattice were analyzed theoretically [7], [8], and recently it was shown both theoretically and experimentally that a slight localized perturbation in the lattice constant of an otherwise uniform photonic crystal waveguide can create a resonant cavity with a quality (Q) factor in excess of 10^5 and mode volume on the order of one cubic wavelength [9], [10]. Since then, there have been reports of forming similar high-Q-factor cavities through other methods of perturbation, including local modulation of a photonic crystal line defect width [11], local air-hole infiltration [12], [13], photosensitive materials [14], effective index change through microfiber coupling [15], and local modulation of the hole radii [16]. We reported that photonic crystal

double-heterostructure bound states always form near local extrema of the associated photonic crystal waveguide dispersion diagram [17], and whether the extreme is a local maximum or a local minimum depends on whether the local perturbation moves the band to a higher or lower frequency. A numerical analysis showed that Q-factors as high as 10^9 are possible with a tapered perturbation [18]. Recent studies have investigated the effect of adding a slot along the center of the photonic crystal waveguide [19], [20].

The ultrahigh Q-factors and cubic wavelength mode volumes along with the waveguide-like shape of the cavities have made them attractive for a variety of applications, including chemical sensing [20], slow light [21], [22], elements of coupled resonator optical waveguides [23], and edge-emitting lasers [24]–[28]. For the case of microcavity semiconductor lasers, the ultrahigh Q provides considerable flexibility in preferentially lowering the total Q via output coupling mechanisms while still maintaining an overall low-loss optical cavity. This flexibility has been exploited to form edge-emitting lasers with output powers among the highest in photonic crystal lasers. However, much remains to be learned about the optical leakage of these cavities to maximize their directional radiation properties. In this paper, we investigate the theoretical properties of photonic crystal double-heterostructure laser cavities by analyzing their Q-factors, field profiles, and radiation patterns. In particular, we discuss higher order bound states, a method of discriminating between higher order bound states for improved side-mode suppression and the suitability of the various modes for laser applications. We include experimental lasing data to support the theoretical observations. In addition to edge-emitting photonic crystal lasers, other technologies that we hope will benefit from this theoretical investigation are photonic crystal double-heterostructure lasers bonded to or grown on heat sinking substrates and design of devices for electrical injection.

II. PHOTONIC CRYSTAL DOUBLE-HETEROSTRUCTURE CAVITIES

Fig. 1 is a top schematic view of a photonic crystal double heterostructure in which the lattice constant (a') of the light colored holes has been stretched along the x-direction. A local increase in the lattice constant shifts the photonic crystal waveguide band to lower frequencies [9], [10], [17]. If the waveguide band has a local minimum, then the perturbation will push the local minimum of the modified region into the mode gap of the neighboring waveguide regions. Because there are no propagating modes in the adjacent waveguides, light is confined along the x-direction. The left portion of Fig. 2 is a photonic crystal waveguide dispersion diagram corresponding to a single line
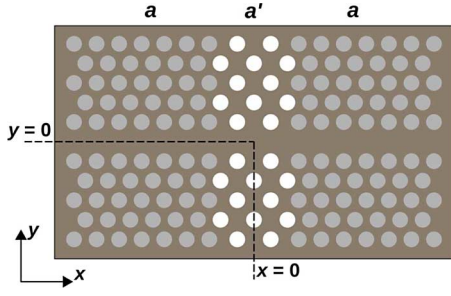
Fig. 1. Schematic top view of a photonic crystal double-heterostructure cavity.
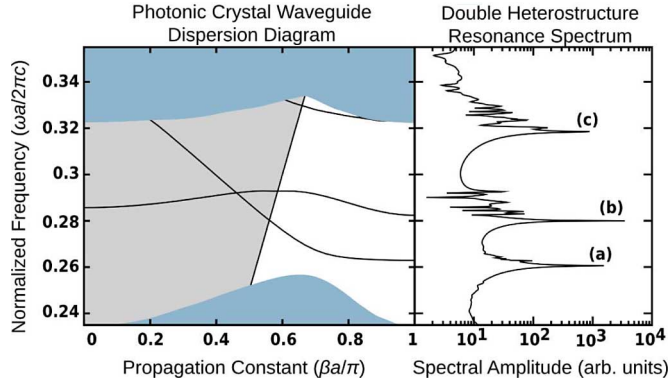

Fig. 2. (Left) Dispersion diagram of a photonic crystal waveguide. (Right) Calculated resonance spectrum for a photonic crystal double-heterostructure cavity. a is the photonic crystal lattice constant and c is the vacuum speed of light.

Fig. 3. $H_z(x, y)$ at the midplane of the slab for the modes labeled (a), (b), and (c) in Fig. 2.

defect with the following parameters: hole radius to lattice constant ratio $r/a = 0.29$, slab thickness to lattice constant ratio $d/a = 0.6$, and index of refraction $n = 3.4$. The black lines in the dispersion diagram correspond to the TE-like waveguide propagating modes and were calculated using the 3-D finite-difference time-domain (FDTD) method [29]. Only a single unit cell of the waveguide was stored in memory, and Bloch boundary conditions were applied at boundaries separated by a. Details of this approach are described in [30] and [31]. The frequencies corresponding to values covering the first Brillouin zone are obtained from discrete Fourier transforms (DFTs) of the time sequences [30], [31]. The shaded regions at the top and bottom of the figure are projections of the TE-like photonic crystal cladding modes onto the waveguide propagation direction and were obtained using a similar 3-D FDTD method with Bloch boundary conditions [32]. The light gray region denotes the projection of the light cone onto the waveguide dispersion diagram.

The right side of Fig. 2 shows a numerically calculated photonic crystal double-heterostructure resonance spectrum whose frequency axis is aligned with the frequency axis of the waveguide dispersion diagram. The hole radius, slab thickness, and slab index of refraction are the same as that used in the waveguide dispersion calculation. The double-heterostructure cavity is formed by a 5% lattice constant stretching similar to that in Fig. 1. We included 20 waveguide periods along the positive and negative x-directions (shaded holes to the right and left of the perturbed white holes centered at $x = 0$ in Fig. 1) and eight
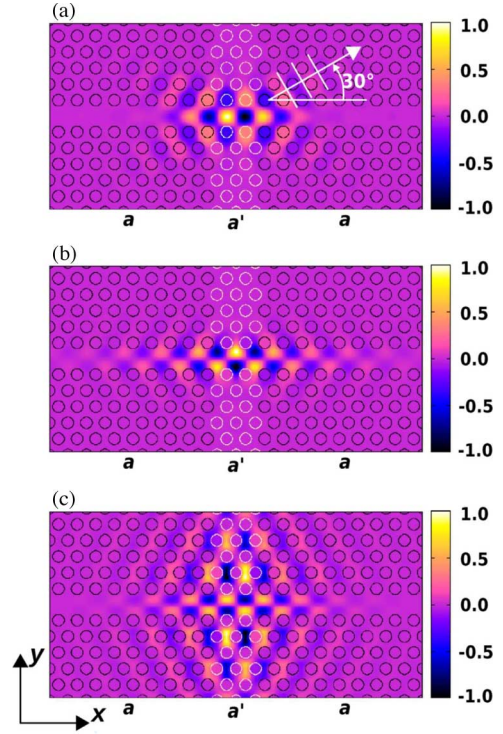
rows of photonic crystal holes along the positive and negative y-directions (above and below the waveguide core centered at $y = 0$ in Fig. 1). We discretized the geometry using 20 points per lattice constant. The computational domain size was (950, 340, 200) points along (x, y, z), which was then parallelized on 132 processors. To prevent reflections due to the computational domain boundary, we include 15 layers of perfectly matched layer absorbing boundary conditions on each boundary [29]. We record 2×10^5 time steps, which corresponds to 25 ps, and to obtain the spectrum in Fig. 2, we perform a DFT of the resulting time sequence. Typical calculations run for approximately 16 h on the University of Southern California High Performance Computing and Communications Beowolf cluster [33].

Comparison between the double-heterostructure resonance spectrum on the right side of Fig. 2 and the waveguide dispersion diagram on the left side indicates that the main resonance peaks are centered at frequencies just below the minima of the waveguide dispersion bands. The other peaks with lower amplitudes that neighbor the bound state resonances are due to Fabry–Perot resonances in the unperturbed waveguide sections of the devices. These peaks have been analyzed in [17].

Fig. 3 illustrates the z-component of the magnetic field at the middle of the slab for the three bound state resonances labeled in Fig. 2. For the TE-like modes, the only nonzero field components at the slab midplane are E_x, E_y, and H_z. We plot the $H_z(x, y)$ component due to the completely scalar nature of the magnetic field at this position.

The spatial distribution of the bound states has the same properties as the underlying waveguide mode distribution multiplied

TABLE I
OPTICAL CONFINEMENT PROPERTIES OF DOUBLE-HETEROSTRUCTURE MODES
FEATURED IN FIGS. 2 AND 3

Mode	Q Factor	$P\perp/P_\parallel$	P_x/P_y
(a)	337,000	1.8	0.2
(b)	10,800	1.2	42.6
(c)	8,300	0.4	0.01

by a confining Gaussian-like envelope function. The mode profiles were obtained from subsequent FDTD runs with a discrete-time filter to isolate the frequency of interest [34]. The mode profiles shown in Fig. 3(a) and (b) exhibit relatively tight in-plane confinement, whereas the mode in Fig. 3(c) displays significant field amplitude deep into the photonic crystal cladding. This can be explained by noting that the frequency of mode (c) in Fig. 2 is just barely below the upper photonic crystal cladding band. Portions of waveguide bands that do not lie inside the bandgap are not confined by the photonic crystal lattice. As the frequency of the waveguide mode approaches the photonic crystal cladding frequencies from inside the bandgap, the cladding gradually ceases to confine the waveguide mode (analogous to approaching the cutoff condition in slab waveguides). Therefore, the decay length into the cladding is expected to be relatively long for this mode. One important conclusion from this analysis is that many properties of double-heterostructure modes can be obtained from the properties of the photonic crystal waveguide from which it is formed.

Table I summarizes the optical confinement properties of the three double-heterostructure modes featured in Figs. 2 and 3. The Q-factor is obtained by measuring the full-width at half maximum (FWHM) of the resonance spectrum shown on the right side in Fig. 2. Because only a finite number of time steps can be obtained, the frequency resolution is limited, and only Q-factors of a few hundred can be reliably extracted from the raw DFT data. To estimate the FWHM corresponding to higher Q-factors from the available data, we use the Padé interpolation method [35] with a direct parameter extraction approach [36]. As the number of time steps used in the FDTD simulation increases, the frequency resolution improves, and one expects that the Q estimation will improve as the time sequence is lengthened. Fig. 4 shows the convergence of the extracted Q-factor values as a function of the number of time steps used in the DFT. The top axis indicates the frequency spacing between adjacent frequency samples, which decreases as the number of time steps used in the DFT increases. In addition to the 5% perturbation double-heterostructure cavity that has been discussed so far, convergence analysis for 2.5% and 7.5% perturbations are presented as well. For each perturbation, the Q-factor has stabilized well before 2×10^5 time steps. However, more time steps are required as the Q-factor increases due to the narrowing of the FWHM.

Table I lists Q-factors that vary significantly among the three modes. To investigate leakage properties of the different modes, we analyzed the Poynting vector components to determine the direction in which the power was leaking. To extract the true propagating energy from the circulating near fields of the cavity,
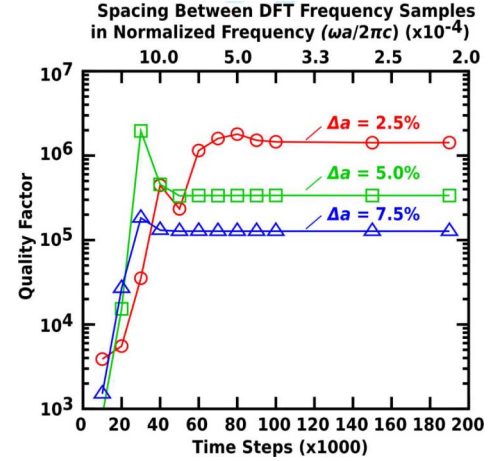

Fig. 4. Extracted Q-factors as a function of time steps used in calculating the DFT. Top axis indicates spacing between frequency samples in the DFT, which is inversely proportional to the number of time steps. a is the photonic crystal lattice constant and c is the vacuum speed of light.

we calculate the time average of the Poynting vector over one optical cycle. For high-Q-factor cavities, only a small amount of energy leaks out of the cavity per optical cycle. To measure this small energy leakage, we use a fine temporal discretization resulting in 50 000 time steps per optical period. To find the directional power flow, the time-averaged Poynting vector is spatially integrated over an appropriate surface. To verify that we have accurately evaluated the time-averaged power flow, we calculate the time-averaged Poynting vector over a closed surface and compare the result to the change in the enclosed energy according to Poynting's theorem and find agreement consistently to within 1%. The third column in Table I lists the ratio of power radiated vertically out of plane to the power that propagates outward but remains inside the semiconductor slab. For modes (a) and (b), the majority of the leakage is out of plane. This confirms our earlier observation that modes (a) and (b) are well confined in plane, and mode (c) shows significant extension into the photonic crystal cladding region. The fourth column lists the ratio of power emitted along the x-direction to the power radiated along y. Mode (a) emits five times more power into the photonic crystal cladding than along the waveguide direction. Examining the $H_z(x, y)$ mode profile in Fig. 3(a) reveals that the field extends into the cladding at angles of $30°$ from the waveguide axis. This can be explained by considering the first Brillouin zone of a 2-D triangular lattice, as shown in Fig. 5. Double-heterostructure resonant modes are primarily made up of wave vector components near the associated waveguide dispersion minima, which occur at $\beta_x = \pi/a$, as shown in Fig. 2. The projection of the photonic crystal cladding modes onto the waveguide dispersion diagram maps an M point to $\beta_x = \pi/a$, as shown in Fig. 5. The waveguide direction corresponds to the $\Gamma - K$ direction in reciprocal space. Because the M point is a $30°$ rotation from the K point in the first Brillouin zone, radiation at $30°$ from the waveguide direction is reasonable.

The in-plane radiation of mode (b) is dominated by radiation along the waveguide direction. In order to understand the reason for this, we broke down the total Q-factor according to $Q^{-1} =$
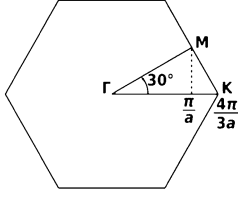
Fig. 5. Illustration of first Brillouin zone for a triangular photonic crystal lattice. High symmetry points are labeled.

TABLE II
BREAKDOWN OF SPATIAL Q-FACTORS OF DOUBLE-HETEROSTRUCTURE MODES FEATURED IN FIGS. 2 AND 3

Mode	Q_x	Q_y	Q_z
(a)	5,960,000	1,120,000	525,000
(b)	24,200	10,300,000	19,900
(c)	83,900	12,100	27,400

$Q_x^{-1} + Q_y^{-1} + Q_z^{-1}$, and used the power flow ratios in Table I to solve for each of the Q-factors. The results for modes (a)–(c) are summarized in Table II. The Q_y for mode (b) is actually the highest Q-factor in Table II, which indicates that mode (b) has the least amount of leakage into the photonic crystal cladding. We attribute this to its central location in the photonic crystal bandgap. This implies that the in-plane collection efficiency for radiation along the waveguide direction is quite large for this mode.

Finally, the in-plane radiation of mode (c) is dominated by radiation into the photonic crystal cladding. Again, the constant phase contours of the radiation front are at a $30°$ angle with respect to the waveguide axis for the same reasons as previously discussed for mode (a).

As a final remark, we would like to comment on the parity along the x-direction of the fields shown in Fig. 3. Specifically, Fig. 3(a) shows that the magnetic field goes through zero at the center of the cavity. Close inspection of Fig. 1 shows that the perturbation is formed by perturbing two holes next to the waveguide core followed by three holes as one moves away from the waveguide core along the y-direction. Alternatively, one may choose to perturb three holes next to the waveguide core followed by two and so on along the y-direction. The $H_z(x, y)$ profile of such a structure is shown in Fig. 6. Note that now the magnetic field is peaked at the center of the cavity. We also find that the Q-factor of this cavity is 366 000, which is about 10% larger than 337 000 for the analogous mode (a), as shown in Table I. The main point is that one may form photonic crystal double-heterostructure cavities in ways that allow for the control of parity along the x-direction while maintaining similar Q-factor values. In general, one should expect an $H_z(x, y)$ field that has odd parity about $x = 0$ for an even number of perturbed holes adjacent to the waveguide core and an $H_z(x, y)$ field that has even parity about $x = 0$ for an odd number of perturbed holes adjacent to the waveguide core. ($x = 0$ and $y = 0$ are denoted in Fig. 1.) Due to the TE-like nature of the electromagnetic fields at the midplane of the slab, the electric field components, E_x and E_y, are related to the magnetic field through simple spatial derivatives according to Maxwell's equations. For instance,
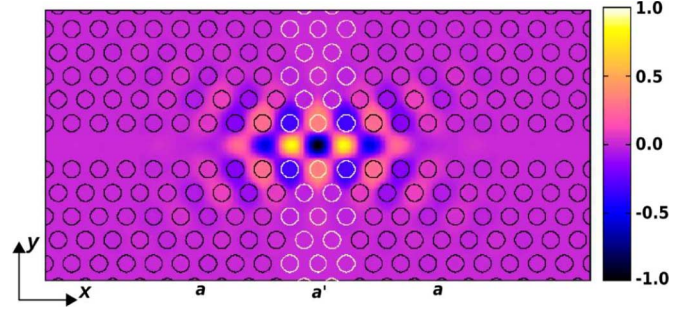

Fig. 6. $H_z(x, y)$ at the midplane of the slab for a double-heterostructure cavity with three perturbed holes adjacent to the waveguide core.
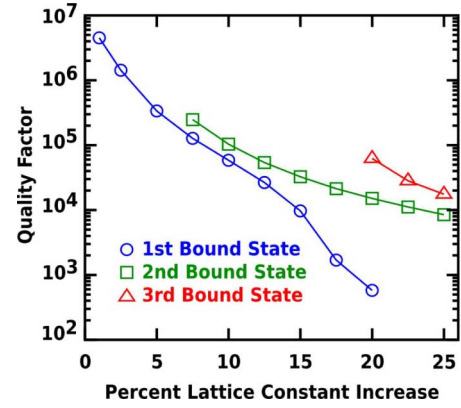

Fig. 7. Q-factor as a function of lattice constant perturbation for first-, second-, and third-order bound states.

because E_x is proportional to $\partial H_z / \partial y$, E_x will have the same parity as H_z about $x = 0$ but opposite parity about $y = 0$. Analogously, because E_y is proportional to $\partial H_z / \partial x$, E_y will have the opposite parity as H_z about $x = 0$ and the same parity about $y = 0$.

III. HIGHER ORDER BOUND STATES

We have already seen in Fig. 4 that the Q-factor decreases as the perturbation in the double-heterostructure cavity is deepened. This trend is explored in the curve labeled "1st Bound State" in Fig. 7 that shows the dependence of the Q-factor of mode (a) in Figs. 2 and 3 on the lattice constant perturbation. As the perturbation is made stronger, the Q-factor drops rapidly. Making the perturbation deeper increases the confinement of the mode in real space, which causes the Fourier space distribution to spread. The spreading in Fourier space causes the portion of the Fourier space distribution overlapping the light cone to increase. This may be seen qualitatively in Fig. 8, which depicts the 2-D spatial Fourier transform of $E_y(x, y)$ for a 5% perturbation on the left and a 15% perturbation on the right. It is clear that there is significantly higher energy inside the light cone for the 15% perturbation.

Although the Q-factor drops rapidly as the perturbation is increased, one sees that higher order modes are supported for sufficiently strong perturbations. Furthermore, for a given perturbation, the highest order mode supported by the cavity has the highest Q-factor. This is a promising approach for obtaining
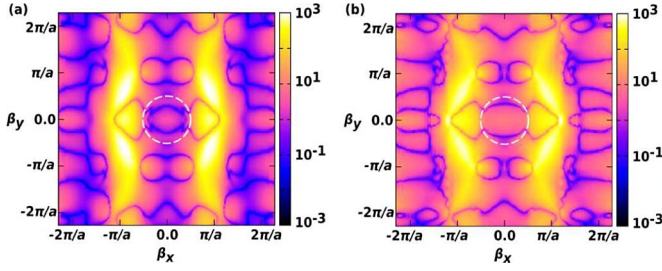
Fig. 8.   2-D spatial Fourier transform of $E_y(x, y)$ at the midplane of the slab of double-heterostructure cavities with (a) 5% and (b) 15% perturbation.
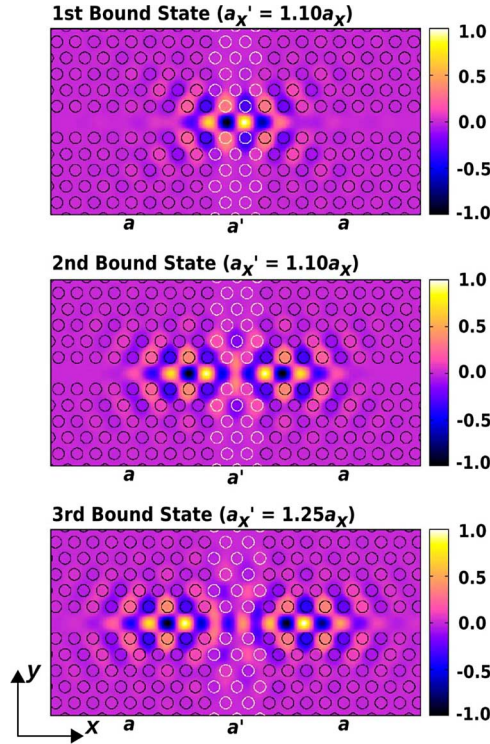

Fig. 9. $H_z(x, y)$ at the midplane of the slab for the first- and second-order bound states of a double-heterostructure cavity with 10% perturbation and the third-order bound state of a double-heterostructure cavity with a 25% perturbation.
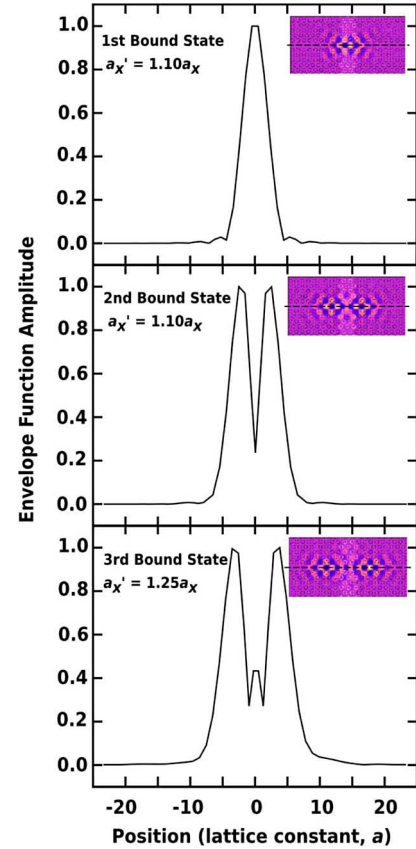

Fig. 10.   Envelope functions for the first-, second-, and third-order bound states in Fig. 9 calculated by measuring the local maxima of $|H_z(x, 0)|$. The insets indicate the linear cut of the field used in obtaining the envelope functions.

high Q-factor modes without requiring extremely small perturbations, which can be difficult to fabricate. Fig. 9 displays the z-component of the magnetic field at the middle of the slab for the first and second bound states corresponding to a double-heterostructure cavity with 10% perturbation and the third-order bound state corresponding to a double-heterostructure cavity with 25% perturbation. Careful inspection of these field profiles shows that the first-order bound state is odd about $x = 0$, the second-order bound state is even about $x = 0$, and the third-order bound state is odd about $x = 0$. In light of the discussion regarding Fig. 6, the parity of each of the modes can be switched by employing a double heterostructure with a perturbation with three holes adjacent to the waveguide core instead of two. In Fig. 10, we plot the envelope function of the field profiles in Fig. 9 by recording the local maxima of $|H_z(x, 0)|$. The envelope functions for the first-, second-, and third-order bound

states have zero, one, and two nodes, respectively. This is consistent with what we expect from the solution of the 1-D quantum well problem in quantum mechanics

IV. MODE DISCRIMINATION

When a cavity supports multiple modes, it can be useful to modify the cavity to enhance one of the modes relative to the others. Following the approach of [37], we have modified the double-heterostructure cavities by adding extra holes at the electric field maxima of the bound state resonance mode that we wish to suppress. Fig. 11(a) is an unmodified double-heterostructure cavity with 10% perturbation. The double-heterostructure cavity shown in Fig. 11(b) includes an additional two holes with $r = 0.2a$ near the maxima of the second-order bound state whose purpose is to suppress the second-order bound state relative to the first-order bound state. In Fig. 11(c), we have added a single hole with $r = 0.2a$ in the middle of the cavity to suppress the first-order bound state relative to the second-order bound state.

Fig. 12 shows the numerically calculated resonance spectra for the three cavities in Fig. 11. The low-frequency peak in the top curve corresponds to the first-order bound state. The next peak on the high-frequency side of the first peak corresponds to the second-order bound state. Ripples on the high-frequency side of the second peak are due to Fabry–Perot resonances in
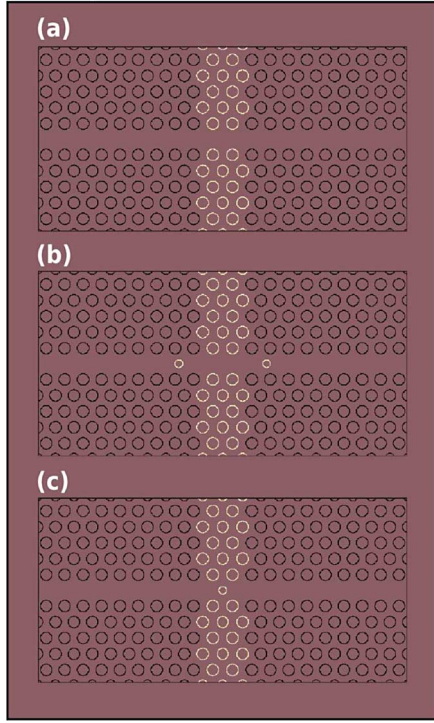
Fig. 11. Double-heterostructure cavities with (a) 10% perturbation; (b) 10% perturbation and two additional holes with $r = 0.2a$ at $x = \pm 2.4a$; and (c) 10% perturbation and an additional hole with $r = 0.2a$ at $x = 0$.
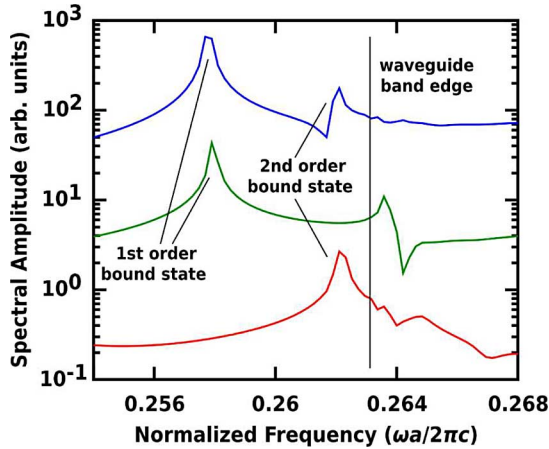

Fig. 12. Numerically calculated resonance spectra for the three double-heterostructure cavities shown in Fig. 11. The top curve corresponds to an unmodified double-heterostructure cavity with $a'_x = 1.10a_x$. The middle curve corresponds to a double-heterostructure cavity with two holes added at $x = \pm 2.4a$. The bottom curve corresponds to a double-heterostructure cavity with a single hole at $x = 0$.

the uniform waveguide sections of the double-heterostructure cavity, as discussed earlier and in [17]. When the two holes are added as in Fig. 11(b), the second-order bound state resonance peak disappears, as depicted in the middle curve in Fig. 12. Similarly, when a single hole is added, the first-order bound state resonance peak disappears, as shown in the bottom curve in Fig. 12.

Fig. 13 shows the dependence of the first-order bound state Q-factor on the distance of the two holes from the center of
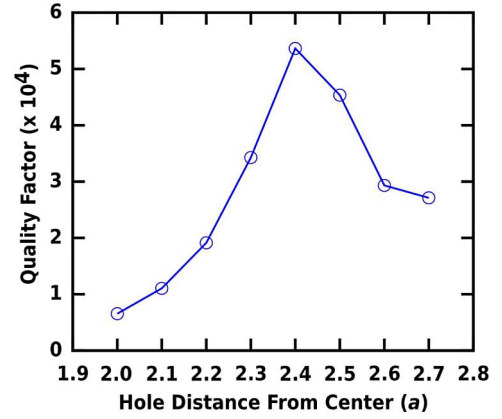

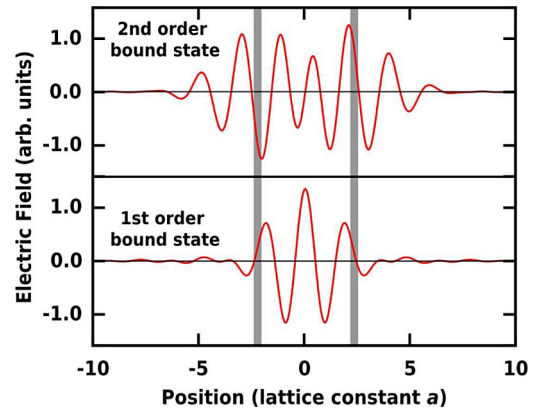Fig. 13. Q-factor as a function of the position of the two holes in Fig. 11(b).

Fig. 14. Illustration of the optimized hole position indicated by the dark bars relative to the y-component of the electric fields of the first- and second-order bound states in an unmodified double-heterostructure cavity.

the cavity. If the extra holes are placed at their optimum distance of $2.4a$ from the center of the cavity along x, then the passive Q-factor of the first-order bound state changes by only about 10% from 58 600 for the unmodified structure to 53 600 for the optimal modified structure. Fig. 14 illustrates the optimal hole placement relative to the E_y field profiles plotted as a function of x along the center of the waveguide for the first- and second-order bound states of an unmodified double-heterostructure cavity. From Fig. 14, one can see that the optimal hole location is near a field maximum for the second-order bound state and a field zero for the first-order bound state. Placing a hole at the center of the cavity changes the Q-factor of the second-order bound state from 104 000 for the unmodified double heterostructure to 123 000 for the modified structure. Explaining the modest increase in the Q-factor starts by noting that adding a hole in the middle of the cavity decreases the effective index of the structure. As the effective index decreases, the resonance frequency increases. However, adding the hole in the perturbed region has a smaller effect on the waveguide band edge frequency of the neighboring uniform waveguide sections. As the bound state resonance frequency increases, the difference between the bound state resonance frequency and the waveguide band edge frequency decreases resulting in a less tightly bound mode. From Figs. 7 and 8, we found that the Q-factor
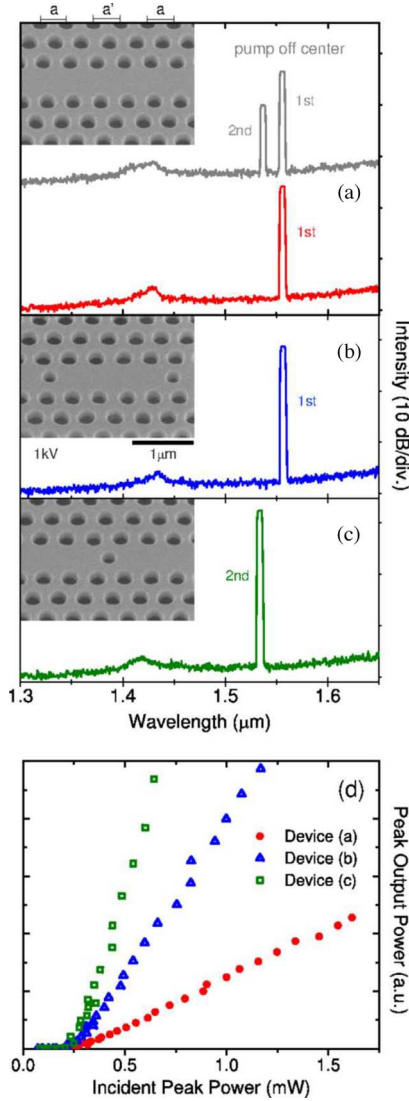
Fig. 15. (a)–(c) Lasing spectra of three double-heterostructure lasers with 10% perturbation ($a'_x = 1.10a_x$). Their SEM images, shown as insets, were taken at the same experimental conditions. (d) is the L-L curves of the lasers in (a)–(c).

increases as the various bound state modes become less tightly bound, and we attribute the increase in Q-factor to this effect.

V. EXPERIMENTAL DEMONSTRATION OF MODE DISCRIMINATION IN DOUBLE-HETEROSTRUCTURE LASERS

To experimentally verify the proposed modified photonic crystal double-heterostructure cavities for preferential selection between the first and second bound states, a set of three double-heterostructure laser cavities were fabricated in a 240-nm-thick suspended InGaAsP membrane containing four compressively strained quantum wells. The semiconductor dry-etch was done in an inductively coupled plasma etcher using BCl_3 chemistry at $165°C$. The rest of the fabrication processes are the same as those in [24]. SEM images of the final devices are shown as insets in Fig. 15(a)–(c), where (a) is the regular double-heterostructure cavity, (b) has two extra holes $2.4a$ away from the device center

along the waveguide core, and (c) has one extra hole placed at the center of the device. The lattice constant (a) is 405 nm and the perturbed lattice constant (a') is 10% larger than a along the waveguide direction in all three devices.

The devices are optically pumped at room temperature by an 850 nm diode laser at normal incidence with an 8 ns pulsewidth and 1% duty cycle. The size of the pump spot is about 2 μm in diameter. The lower spectrum in Fig. 15(a) is the single-mode lasing spectrum operating in the first bound state, while the upper multimode lasing spectrum shows the existence of the second bound state approximately 20 nm away from the first one when the pump spot is slightly moved off the device center along the waveguide core. This wavelength separation is smaller than the predicted spacing of 25 nm from the 3-D FDTD calculation. We explain this discrepancy by noting that the standard deviation of the lattice constant in the device is about 2% as analyzed from SEM images, which effectively weakens the effect of a 10% lattice constant perturbation. Another possible cause of this discrepancy could be attributed to material dispersion, which was not included in our FDTD simulation. The two modified structures in Fig. 15(b) and (c) are both stable in single-mode operation against the pump offsets. Their lasing wavelengths line up with the first and second bound states lasing in the nonmodified structure. All four lasing spectra were taken at the peak incident power of 1.7 mW. The broad resonance peak between 1.40 and 1.45 μm corresponds to the second waveguide dispersion band shown in Fig. 2. Fig. 15(d) depicts the light-in–light-out (L-L) curves of the three lasers described before. They have almost identical thresholds but different slopes, indicating the same amount of total optical loss but different portions of collected laser power. Devices (a) and (b) have the same lasing modes and thresholds, but device (b) has a higher slope efficiency. This is likely due to the increased out-of-plane optical loss introduced by the two extra holes, which, in the fabricated device, have radii about 30% larger than what was analyzed numerically before.

These two modified double-heterostructure laser cavities are good complements to the original double-heterostructure cavity for laser applications. The two extra holes can effectively enhance the side-mode suppression ratio [37] for the first bound state against side modes that include not only the higher order bound states but also the low-group-velocity waveguide modes [38]. This design approach will be important for monolithic integration of double-heterostructure lasers with waveguides. The Q-factor of the double-heterostructure mode will decrease by coupling light into an adjacent waveguide [26].

Furthermore, the removal of absorption through quantum well intermixing [28] or regrowth [39] will lower the absorption loss of the side modes that have larger mode volumes. These two issues make it more difficult to obtain single-mode laser operation; therefore, mechanisms to suppress the side modes are essential.

The extra central hole secures the laser to operate in the second bound state, which not only has an even higher passive Q than the first bound state but also a node in the field intensity at the center of the cavity. This might be a candidate for a

photonic crystal laser designed with a current-passing central post underneath for electrical injection [40].

VI. CONCLUSION

This paper discusses several theoretical properties of photonic crystal double-heterostructure resonant cavities. The spatial mode profiles of double-heterostructure bound state resonances associated with different photonic crystal waveguide bands are presented, and their Q-factors and optical leakage properties are analyzed. Field profiles and issues of field parity are discussed. We report on the field profiles and Q-factors of higher order bound states and investigate methods of suppressing unwanted bound states. Finally, we present experimental lasing data illustrating the mode discrimination approach.

REFERENCES

[1] C. Zhang, F. Qiao, J. Wan, and J. Zi, "Large frequency range of neglible transmission in one-dimensional photonic quantum well structures," *Appl. Phys. Lett.*, vol. 73, no. 15, pp. 2084–2086, 1998.

[2] N. Stefanou, V. Yannopapas, and A. Modinos, "Heterostructures of photonic crystals: Frequency bands and transmission coefficients," *Comput. Phys. Commun.*, vol. 113, pp. 39–77, 1998.

[3] C. Zhang, F. Qiao, J. Wan, and J. Zi, "Enlargement of nontransmission frequency range in photonic crystals by using multiple heterostructures," *J. Appl. Phys.*, vol. 87, no. 6, pp. 3174–3176, 2000.

[4] A. Sharkawy, S. Shi, and D. W. Prather, "Heterostructure photonic crystals: Theory and applications," *Appl. Opt.*, vol. 41, no. 34, pp. 7245–7253, 2002.

[5] B.-S. Song, T. Asano, Y. Akahane, Y. Tanaka, and S. Noda, "Transmission and reflection characteristics of in-plane hetero-photonic crystals," *Appl. Phys. Lett.*, vol. 85, no. 20, pp. 4591–4593, 2004.

[6] L. Wu, M. Mazilu, J.-F. Gallet, and T. F. Krauss, "Dual lattice photonic crystal beam splitters," *Appl. Phys. Lett.*, vol. 86, pp. 211106-1–211106-3, 2005.

[7] E. Istrate, M. Charbonneau-Lefort, and E. H. Sargent, "Theory of photonic crystal heterostructures," *Phys. Rev. B*, vol. 66, pp. 075121-1–075121-6, 2002.

[8] E. Istrate and E. H. Sargent, "Photonic crystal heterostructures—Resonant tunnelling, waveguides and filters," *J. Opt. A*, vol. 4, pp. S242–S246, 2002.

[9] B.-S. Song, S. Noda, T. Asano, and Y. Akahane, "Ultra-high-Q photonic double-heterostructure nanocavity," *Nature Mat.*, vol. 4, pp. 207–210, 2005.

[10] B.-S. Song, T. Asano, and S. Noda, "Heterostructures in two-dimensional photonic-crystal slabs and their application to anocavities," *J. Phys. D*, vol. 40, pp. 2629–2634, 2007.

[11] E. Kuramochi, M. Notomi, S. Mitsugi, A. Shinya, and T. Tanabe, "Ultrahigh-Q photonic crystal nanocavities realized by the local width modulation of a line defect," *Appl. Phys. Lett.*, vol. 88, pp. 041112-1–041112-3, 2006.

[12] S. Tomljenovic-Hanic, C. M. de Sterke, and M. J. Steel, "Design of high-Q cavities in photonic crystal slab heterostructures by air-holes infiltration," *Opt. Exp.*, vol. 14, no. 25, pp. 12451–12456, 2006.

[13] C. L. C. Smith, D. K. C. Wu, M. W. Lee, C. Monat, S. Tomljenovic-Hanic, C. Grillet, B. J. Eggleton, D. Freeman, Y. Ruan, S. Madden, B. Luther-Davies, H. Giessen, and Y.-H. Lee, "Microfluidic photonic crystal double heterostructures," *Appl. Phys. Lett.*, vol. 91, pp. 121103-1–121103-3, 2007.

[14] S. Tomljenovic-Hanic, M. J. Steel, C. M. de Sterke, and D. J. Moss, "High-Q cavities in photosensitive photonic crystals," *Opt. Lett.*, vol. 32, no. 5, pp. 542–544, 2007.

[15] M.-K. Kim, I.-K. Hwang, M.-K. Seo, and Y.-H. Lee, "Reconfigurable microfiber-coupled photonic crystal resonator," *Opt. Exp.*, vol. 15, no. 25, pp. 17241–17247, 2007.

[16] S.-H. Kwon, T. Sünner, M. Kamp, and A. Forchel, "Ultrahigh-Q photonic crystal cavity created by modulating air hole radius of a waveguide," *Opt. Exp.*, vol. 16, no. 7, pp. 4605–4614, 2008.

[17] A. Mock, L. Lu, and J. D. O'Brien, "Spectral properties of photonic crystal double heterostructure resonant cavities," *Opt. Exp.*, vol. 16, no. 13, pp. 9391–9397, 2008.

[18] Y. Tanaka, T. Asano, and S. Noda, "Design of photonic crystal nanocavity with Q-factor of 10^9," *J. Lightw. Technol.*, vol. 26, no. 11, pp. 1532–1539, Jun. 2008.

[19] T. Yamamoto, M. Notomi, H. Taniyama, E. Kuramochi, Y. Yoshikawa, Y. Torii, and T. Kuga, "Design of a high-Q air-slot cavity based on a width-modulated line-defect in a photonic crystal slab," *Opt. Exp.*, vol. 16, no. 18, pp. 13809–13817, 2008.

[20] S.-H. Kwon, T. Sünner, M. Kamp, and A. Forchel, "Optimization of photonic crystal cavity for chemical sensing," *Opt. Exp.*, vol. 16, no. 16, pp. 11709–11717, 2008.

[21] Y. Takahashi, H. Hagino, Y. Tanaka, B.-S. Song, T. Asano, and S. Noda, "High-Q nanocavity with a 2-ns photon lifetime," *Opt. Exp.*, vol. 15, no. 25, pp. 17206–17213, 2007.

[22] T. Tanabe, M. Notomi, E. Kuramochi, A. Shinya, and H. Taniyama, "Trapping and delaying photons for one nanosecond in an ultrasmall high-Q photonic-crystal nanocavity," *Nature Photon.*, vol. 1, pp. 49–52, 2007.

[23] D. O'Brien, M. D. Settle, T. Karle, A. Michaeli, M. Salib, and T. F. Krauss, "Coupled photonic crystal heterostructure nanocavities," *Opt. Exp.*, vol. 15, no. 3, pp. 1228–1233, 2007.

[24] M. H. Shih, W. Kuang, A. Mock, M. Bagheri, E. H. Hwang, J. D. O'Brien, and P. D. Dapkus, "High-quality-factor photonic crystal heterostructure laser," *Appl. Phys. Lett.*, vol. 89, pp. 101104-1–101104-3, 2006.

[25] M. H. Shih, A. Mock, E. H. Hwang, W. Kuang, J. D. O'Brien, and P. D. Dapkus, "Photonic crystal heterostructure laser with lattice-shifted cavity," presented at the Tech. Dig. Lasers Electro-Opt., Long Beach, CA, 2006, Paper CMKK3.

[26] T. Yang, S. Lipson, A. Mock, J. D. O'Brien, and D. G. Deppe, "Edge-emitting photonic crystal double-heterostructure nanocavity lasers with InAs quantum dot active material," *Opt. Lett.*, vol. 32, no. 9, pp. 1153–1155, 2007.

[27] L. Lu, T. Yang, A. Mock, M. H. Shih, E. H. Hwang, M. Bagheri, A. Stapleton, S. Farrell, J. D. OBrien, and P. D. Dapkus, "100 μW edge-emitting peak power from a photonic crystal double-heterostructure laser," presented at the Tech. Dig. Laser Electro-Opt., Baltimore, MD, 2007, Paper CMV3.

[28] L. Lu, A. Mock, M. Bagheri, E. H. Hwang, J. O'Brien, and P. D. Dapkus, "Double-heterostructure photonic crystal lasers with reduced threshold pump power and increased slope efficiency obtained by quantum well intermixing," *Opt. Exp.*, vol. 16, pp. 17342–17347, 2008.

[29] A. Taflove and S. C. Hagness, *Computational Electrodynamics*. Norwood, MA: Artech House, 2000.

[30] W. Kuang, C. Kim, A. Stapleton, W. J. Kim, and J. D. O'Brien, "Calculated out-of-plane transmission loss for photonic-crystal slab waveguides," *Opt. Lett.*, vol. 28, no. 19, pp. 1781–1783, 2003.

[31] W. Kuang, W. J. Kim, A. Mock, and J. D. OBrien, "Propagation loss of line-defect photonic crystal slab waveguides," *IEEE J. Sel. Topics Quantum Electron.*, vol. 12, no. 6, pp. 1183–1195, Nov./Dec. 2006.

[32] W. Kuang, W. J. Kim, and J. D. O'Brien, "Finite-difference time domain method for nonorthogonal unit-cell two-dimensional photonic crystals," *J. Lightw. Technol.*, vol. 25, no. 9, pp. 2612–2617, Sep. 2007.

[33] (2004). [Online]. Available: http://www.usc.edu/hpcc/

[34] A. Oppenheim and R. Schafer, *Discrete-Time Signal Processing*. Upper Saddle River, NJ: Prentice-Hall, 1999.

[35] S. Dey and R. Mittra, "Efficient computation of resonant frequencies and quality factors of cavities via a combination of the finite-difference time-domain technique and the Padé approximation," *IEEE Microw. Guided Wave Lett.*, vol. 8, no. 12, pp. 415–417, Dec. 1998.

[36] A. Mock and J. D. O'Brien, "Convergence analysis of Padé interpolation for extracting large quality factors in photonic crystal double heterostructure resonant cavities," in *Proc. Tech. Dig. Numer. Simul. Optoelectron. Devices*, 2008, Paper TuB3, pp. 57–58.

[37] W. Kuang, R. Cao, S.-J. Choi, J. D. OBrien, and P. D. Dapkus, "Modied suspended membrane photonic crystal D3 laser cavity with improved sidemode suppression ratio," *IEEE Photon. Technol. Lett.*, vol. 17, no. 5, pp. 941–943, May 2005.

[38] K. Kiyota, T. Kise, N. Yokouchi, T. Ide, and T. Baba, "Various low group velocity effects in photonic crystal line defect waveguides and their demonstration by laser oscillation," *Appl. Phys. Lett.*, vol. 88, no. 20, pp. 201904-1–201904-3, 2006.

[39] K. Nozaki, H. Watanabe, and T. Baba, "Photonic crystal nanolaser monolithically integrated with passive waveguide for effective light extraction," *Appl. Phys. Lett.*, vol. 92, no. 2, pp. 021108-1–021108-3, 2008.

[40] H. G. Park, S. H. Kim, S. H. Kwon, Y. G. Ju, J. K. Yang, J. H. Baek, S. B. Kim, and Y. H. Lee, "Electrically driven single-cell photonic crystal laser," *Science*, vol. 305, no. 5689, pp. 1444–1447, 2004.

Adam Mock (S'08) received the B.S. degree in electrical engineering from Columbia University, New York, in 2003. He is currently working toward the Ph.D. degree in electrical engineering at the University of Southern California (USC), Los Angeles.

His current research interests include microphotonic device simulation and analysis.

Ling Lu (S'09) received the B.S. degree in physics from Fudan University, Shanghai, China, in 2003, and the M.A. degree in physics and the M.S. degree in electrical engineering in 2006 and 2007, respectively, from the University of Southern California (USC), Los Angeles, where he is currently working toward the Ph.D. degree in electrical Engineering.

His current research interests include nanophotonics and microcavity laser applications.

Eui Hyun Hwang received the Ph.D. degree in electrical engineering from the University of Southern California, Los Angeles, in 2007.

He currently manages the strategic business group at Samsung, Seoul, Korea.

John O'Brien (M'98–SM'02) received the B.S. degree in electrical engineering from Iowa State University, Ames, in 1991, and the M.S. and Ph.D. degrees in applied physics from California Institute of Technology, Pasadena, in 1993 and 1996, respectively.

In 1997, he was an Assistant Professor at the University of Southern California, Los Angeles, where he was named a Full Professor of electrical engineering-electrophysics in 2006, and is currently the Senior Associate Dean for Academic Affairs at the Viterbi School of Engineering. His current research interests include nanophotonics and photonic crystal devices.

Dr. O'Brien received the Presidential Early Career Award for Scientists and Engineers in 1999 and the National Science Foundation (NSF) Career Award in 2000. He became a Fellow of the Optical Society of America (OSA) in 2007.

P. Daniel Dapkus (SM'80–F'87) received the B.S., M.S., and Ph.D. degrees from the University of Illinois at Urbana-Champagne, in 1966, 1968, and 1970, respectively.

He was a member of the Technical Staff at Bell Laboratories, where he worked on visible LEDs. He then worked at Rockwell International, where he led the group responsible for the demonstration of the viability of metal–organic chemical vapor deposition (MOCVD) as a device epitaxy process. He is currently the William M. Keck Professor of Engineering at the University of Southern California, Los Angeles, where he is engaged in the invention and demonstration of novel and high-performance photonic devices.

Prof. Dapkus was elected to the National Academy of Engineering in 2004.